Ultrathin silver films on Ni(111)

Axel Meyer,[1] J. Ingo Flege,[1,*] Robert E. Rettew,[2] Sanjaya D. Senanayake,[3] Thomas Schmidt,[1] Faisal M. Alamgir,[2] and Jens Falta[1]

[1]*Institute of Solid State Physics, University of Bremen, Otto-Hahn-Allee 1, 28359 Bremen, Germany*

[2]*School of Materials Science and Engineering, Georgia Institute of Technology, Atlanta, Georgia 30332, USA*

[3]*Chemistry Department, Brookhaven National Laboratory, Upton, New York 11973, USA*

(Received 30 April 2010; revised manuscript received 19 July 2010; published 16 August 2010)

The growth and atomic structure of ultrathin silver films on Ni(111) was investigated by low-energy electron microscopy and diffraction (LEEM/LEED) as well as intensity-voltage [$I(V)$]-LEEM in the growth temperature range between 470 and 850 K. We find that silver grows in a Stranski-Krastanov mode with a two monolayer thin wetting layer which takes on a $p(7\times7)$ reconstruction at temperatures lower than 700 K and a $(\sqrt{52}\times\sqrt{52})R13.9°$ reconstruction at higher temperatures. The occurrence of the two distinct reconstructions is shown to have profound implications for the growth characteristics of films exhibiting thicknesses of one and two monolayers. The nanoscale $I(V)$ characteristics of the films were analyzed by means of multiple-scattering calculations based on dynamical LEED theory. Furthermore, the vertical interatomic spacing at the interface between the Ag film and the Ni substrate was determined to (2.8 ± 0.1) Å for all film thicknesses (<13 ML) while the uppermost silver layer relaxes by about $(4\pm1)\%$ toward the crystal.

DOI: 10.1103/PhysRevB.82.085424 PACS number(s): 68.37.Nq, 68.55.A−, 68.35.bd, 68.65.−k

I. INTRODUCTION

Ultrathin films on the order of a few atomic layers have come to represent an important focus of research, arising from the dependence of unique physical and chemical properties on layer thickness.[1] These phenomena make them very attractive prototypical model materials for a number of applications including heterogeneous catalysis, storage devices, fuel cells, and optoelectronics. In general, the qualitatively distinct behavior of ultrathin films is related to both structural and electronic modifications of the (usually well known) bulk structure, resulting on one hand from geometrical and chemical constraints at the interface between the film and the substrate material and on the other from quantum confinement imposed by the lowered dimensionality in the direction perpendicular to the interface. While it is evident that this complex interplay is highly material dependent and influenced by the deposition technique, Ag/Ni may be regarded as a model system because the two metals are virtually immiscible[2] and crystallize in the face-centered cubic structure, making it possible to prepare in situ ordered Ag(111)-oriented overlayers on Ni(111) with a sharp interface by molecular-beam epitaxy under ultrahigh-vacuum (UHV) conditions.[3] Usually, the situation is more complex even if nominally immiscible metals are considered, as demonstrated by several studies targeting a variety of related bimetallic systems, e.g., X/Ni [X=Cu,[4,5] Au (Refs. 6–8)] and Ag/X [X=Cu,[9,10] Ru,[11] Fe,[12] and W (Ref. 13)]. In the case of, e.g., Au/Ni(110), the formation[7] of a surface alloy and its subsequent destabilization upon higher Au coverages,[14] was observed at room temperature already, while for Cu/Ni(100) (Ref. 4) alloying was only witnessed for deposition at temperatures T exceeding 570 K.

In addition to chemical considerations, the lattice mismatch of the two materials and its accommodation at their interface, possibly involving the formation of long-range reconstructions of the atoms in the interface region, have a strong influence on the prevailing growth mode, ranging from a layer-by-layer fashion [Ag/Ru(0001) (Ref. 11) and Ag/Fe(100) (Ref. 15) for flat Fe surfaces] to a Stranski-Krastanov-type [Ag/Cu(111),[9] Ag/Fe(110),[12] and Cu/Ni(100) (Ref. 5)]. In the present case of Ag/Ni(111), the lattice mismatch amounts to about 16%, virtually identical to the related system of Au/Ni(111), for which regular arrays of misfit dislocations[8] and stacking-fault formation (Au$[\bar{1}\bar{1}2]\|$Ni$[11\bar{2}]$) (Ref. 16) were reported, clearly emphasizing the need for a precise characterization of the structure at the interface.

Although it has been demonstrated that the interfacial structure has considerable influence on the interaction and electronic coupling between the silver film and the nickel substrate, experimental reproducibility has proven difficult, resulting in contradictory findings from different groups and considerable debate in the very recent literature[17–21] regarding the layer distance of the first Ag monolayer to the Ni substrate. Furthermore, or perhaps consequently, there still is disagreement regarding the growth characteristics of Ag films on Ni(111) at room temperature and elevated temperatures,[17,22,23] including the contentious transition from single to simultaneous double Ag layer growth. In this article, we present a comprehensive study of the Ag/Ni(111) system using a powerful combination of *in situ* experimental techniques involving low-energy electron microscopy (LEEM) and diffraction (LEED) as well as photoemission electron microscopy (PEEM), facilitating a study of the temperature-dependent growth phenomena and the resulting film characteristics on the nanometer scale over a wide range of preparation conditions. Furthermore, by theoretical modeling of the dependence of the electron reflectivity on the kinetic electron energy—the so-called intensity-voltage (I-V) curve—within the framework of dynamical LEED theory we are able to probe the local atomic structure of the silver film and determine the layer spacings both within the silver film and at the interface to the nickel substrate for distinct indi-

vidual film thicknesses. This synergistic approach of *in situ* microscopy, microspectroscopy, diffraction, and theoretical modeling allows us to disentangle thermodynamically and kinetically driven growth phenomena and reconcile previously observed discrepancies to reach a complete and coherent picture of the system.

II. EXPERIMENTAL

The LEEM measurements were performed in a commercial Elmitec spectroscopic photoemission-LEEM installed at beamline U5UA of the National Synchrotron Light Source (NSLS) at Brookhaven National Laboratory (BNL), Upton, NY (USA), allowing *in situ* microscopy with either low-energy electrons or photons from the storage ring.[24]

The substrate we used for the experiments is a commercially purchased, polished Ni(111) single crystal (Mateck) with a nominal orientation better than 0.1°. After insertion into the UHV chamber the sample was cleaned by several cycles of 0.5 keV Ar^+ ion sputtering followed by thermal annealing at 1050 K. Surface morphology and composition after this procedure was checked by LEEM, LEED, and x-ray photoelectron spectroscopy (XPS). The XPS study was performed at beamline U12A of the NSLS. In addition, short flashes to 1300 K were found to improve the smoothness of the surface on the micrometer scale.

Silver was deposited from a Knudsen cell employing resistive heating of a crucible filled with high-purity Ag (99.9999%, Johnson Mathey Compound Co.). The evaporator was equipped with a manual shutter, water cooling, and the flux stability was asserted using a quartz oscillator.

III. COMPUTATIONAL

For the comparison of experimental LEEM intensity-voltage data with theoretical calculations dynamical LEED theory was used. This approach facilitates an accurate determination of the geometrical structure and chemical composition of the topmost layers of a system consisting of a two-dimensional periodic surface slab and an underlying semi-infinite bulk crystal.

The computation was done using the TensErLEED software package designed by Blum and Heinz.[25] The package allows for a fully dynamical calculation of LEED intensity reference spectra for any periodic surface structure. By expanding the atomic scattering matrix in a perturbative approach ("Tensor LEED") it is possible to calculate the geometrical, vibrational, and chemical displacements from a given reference structure efficiently. The optimal set of parameters is determined within a global search algorithm by minimizing the difference between experimental and theoretical $I(V)$ spectra as quantified by the reliability factor (R_2 factor), which has been shown to yield reliable results in recent $I(V)$-LEEM analyses.[26]

For the quality of the resulting reference calculation, the correct choice of the real and imaginary part of the inner potential of the model system plays an important role. Due to the low-energy range of 2–30 eV used in this work, both parts were treated as separate constants at the low-energy and the high-energy side, reflecting the individual elemental properties. A smooth transition is realized by assuming an "arc tangent"-like energy dependence in the intermediate energy range. This empirical model takes into account the decrease in the probing depth with increasing kinetic energy due to an increased number of possible inelastic interactions, e.g., excitation of plasmons, resulting in more frequent energy losses and thereby more effective damping of the wavefield inside the crystal.

IV. RESULTS AND DISCUSSION

The LEEM, LEEM-$I(V)$, and LEED investigations were conducted at sample temperatures between 470 and 850 K during or after evaporation of silver.

A. Growth mode and characteristics

The Ag growth on the Ni(111) surface was observed in situ with LEEM for an electron energy range between 2 and 7 eV. In this range the oscillations in the reflected intensity with increasing beam energy are very strong due to the quantum size effect (QSE) and as a result of that it is feasible to differentiate Ag layers of distinctive thicknesses because of the large intensity differences, i.e., regions of different brightness, in LEEM images.[27]

The initial growth of silver on Ni(111) is displayed in Fig. 1 with two subsequently recorded images for each temperature. At relatively low temperatures of 500 K or below, silver islands nucleate on the flat Ni terraces, exhibiting only very small correlation with step edges and step bunches [Fig. 1(a)]. Sequentially, these little islands coalesce, leading to the formation of large coherent islands [Fig. 1(b)]. However, the situation is changed at elevated temperatures of about 700 K, where silver preferentially adsorbs at the (lower side[18] of) step edges and step bunches, followed by subsequent nucleation and growth of islands [Fig. 1(c)], which spread over the terraces. In the LEEM image displayed in Fig. 1(d), almost all steps are decorated but the large terrace, which lies close to the mesa in the middle of the micrograph, does not show any signs of silver island growth. Nevertheless, short terraces exhibiting a width in the order of a few tens of nanometers are already covered by a Ag monolayer. Finally, temperature of about 850 K, which is very close to the desorption temperature of Ag from Ni(111) ($T_{des} \approx 890$ K),[23] lead to complete decoration [Fig. 1(e)] of the step edges by silver before island nucleation is witnessed [Fig. 1(f)].

On sufficiently large terraces the growth of the first layer occurs in dendritic (or "fractal") fashion at temperatures of $T < 800$ K (cf. Fig. 2). In general, this phenomenon may have a number of different physical origins, whose prevalence is determined by the peculiarities of the system. Conceptually, the underlying mechanisms may be grouped into categories related to either kinetics or thermodynamics as the major driving forces. In the former case, again different scenarios are generally possible that can be related to the values or ratios of the relevant adatom diffusion lengths. For example, if the capture rate of the islands is larger than the

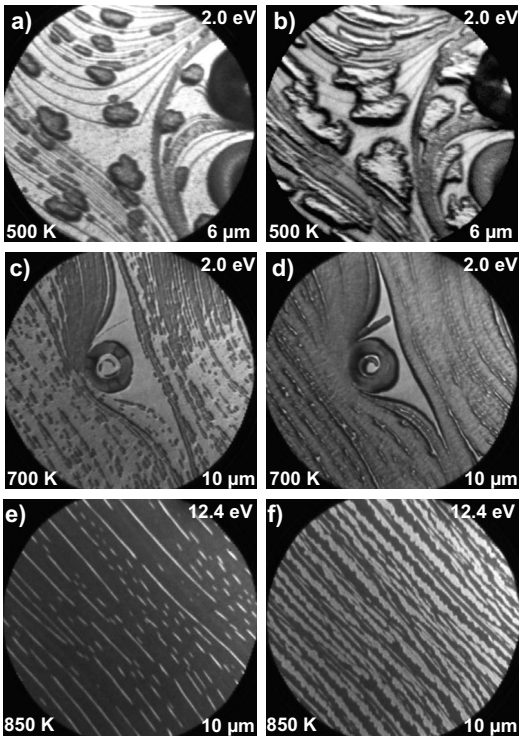

FIG. 1. Initial stages of submonolayer silver growth on Ni(111). In (a) and (b) the first silver layer (dark regions) grows on the flat terraces in single islands at 500 K. These images were taken at 2 eV electron energy and 6 μm field of view (FOV). In (c) and (d), at 700 K and 10 μm FOV, the silver islands (dark) nucleate at steps, which then spread across the terraces. At 850 K the silver (bright) grows preferentially along the step edges in thin lines [images (e) and (f)]. These images were taken at an electron energy of 12.4 eV with 10 μm FOV. The dark round objects in (a)–(d) are insular mesas of the Ni surface. Depending on energy, the silver islands show up bright or dark in contrast.

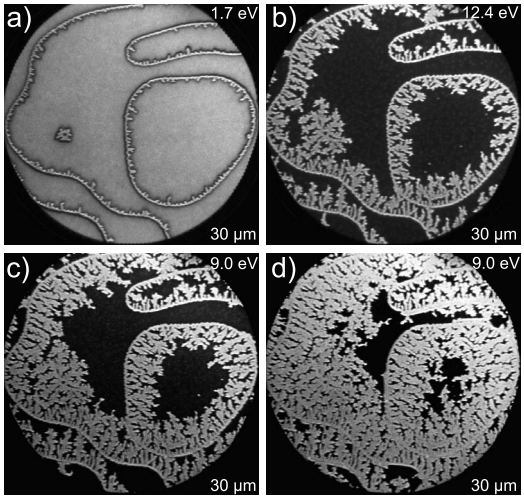

FIG. 2. Dendritical structure of the silver islands (bright) observed during growth on Ni(111) at 750 K and 30 μm FOV *in situ* as visible in LEEM.

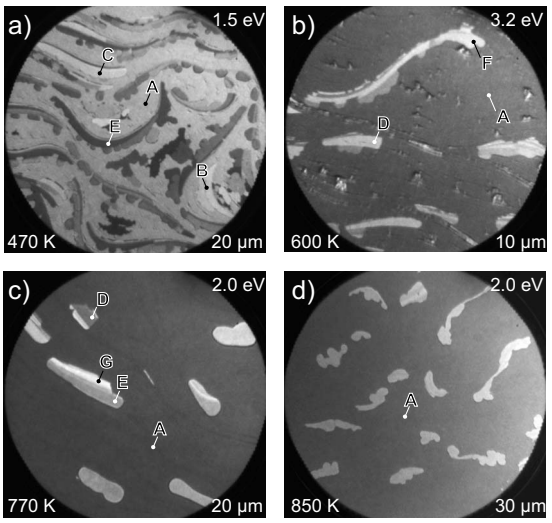

FIG. 3. LEEM images of multilayer silver growth on Ni(111) at temperatures of 470, 600, 770, and 850 K. An increase in uniformity of silver film thickness is visible with increasing temperature. Local film thicknesses: (a) 2 ML, (b) 5 ML, (c) 6 ML, (d) 7 ML, (e) 9 ML, (f) 10 ML, and (g) 12 ML.

diffusion rate along the step edges of the islands, then dendritical island shapes are formed, a concept that has been termed diffusion-limited aggregation[28,29] (and also called "hit and stick") and which readily explains observations in metal-on-metal heteroepitaxy[30] and homoepitaxy.[31] Additionally, dendritic island growth may occur due to anisotropies in diffusion ("hit and jump"), e.g., along step edges aligned in different crystallographic directions in the case of trigonal symmetry.[32–34] In case of thermodynamics as the major driving force, a ramified island shape can also be regarded as the direct consequence of the misfit-induced strain in the overlayer, which is partly relaxed at step edges. The prevalence of this mechanism implies that the amount of strain energy associated with the accommodation and eventual reconstruction of the adlayer to the substrate lattice, which increases with the island area, is higher than the energy cost related to the formation of step edges (the "line energy"), which scales only linearly with the island perimeter, leading to a diversion from a compact island shape.[35] In our example of Ag/Ni growth, we will attribute the observed formation of dendrites to the latter, strain-driven mechanism, for reasons given later in the text. As a first indication for a thermodynamically governed process, we note that we even observe these features at temperatures of up to 750 K that would be extraordinarily high for diffusion-limited phenomena at metal surfaces, which typically happen at significantly lower temperatures due to the smaller differences in the activation barriers involved.

Up to coverages of two monolayers (ML) the growth occurs in a layer-by-layer mode at all temperatures explored in our study. The local film thickness is determined by LEEM-$I(V)$ measurements in combination with $I(V)$ calculations. These results, along with a quantitative analysis of the atomic layer spacings, will be described in detail in Sec. IV C. For growth of a third monolayer on top of the 2-ML wetting layer, the growth characteristics gradually vary with

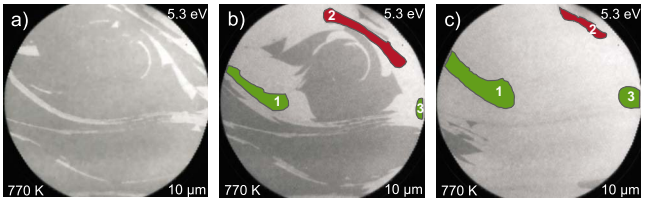

FIG. 4. (Color online) Dewetting of the third silver layer. In (a) the growth of the third silver layer (dark) on the two monolayer silver film (bright) is mostly completed. At this point dewetting (b) sets in, resulting in three-dimensional island growth (islands labeled by 1, 2, and 3). At (c) the third layer is mostly gone and, in addition, island 2 shrinks to cover the thicker islands 1 and 3.

temperature (cf. Fig. 3). Comparatively low temperatures of 470 K [Fig. 3(a)] lead to simultaneous island growth of different thickness on the 2-ML thick wetting layer. At 600 K [Fig. 3(b)], the number of coexisting islands with different thicknesses decreases. Likewise, the island density decreases, which is accompanied by island thickening. This trend continues with increasing temperature [Fig. 3(c)], until uniformity of silver island thickness is attained [Fig. 3(d)] close to the desorption temperature, where Ag mobility is maximal. Hence, the growth of silver on Ni(111) can essentially be described to follow a Stranski-Krastanov-type mode throughout the investigated temperature range, with a wetting-layer thickness corresponding to two atomic Ag layers. These findings also point toward a strain-mediated mechanism as the driving force for the film morphology and island shape observed. An analogous growth behavior has been reported for Ag/Cu(111) (Ref. 10) and Ag/Fe(110),[12] respectively. For these systems, silver grows in the Stranski-Krastanov mode with a wetting layer consisting of two ML at room temperature.

However, for silver growth at elevated temperatures of 600 and 770 K a distinctive feature can be observed (Fig. 4). At both temperatures the third silver layer starts to grow in a layer-by-layer mode [Fig. 4(a)]. At a critical coverage or after stopping deposition the third layer starts to disintegrate and the free silver atoms segregate to existing islands (labeled by 1, 2, and 3) on the surface [Fig. 4(b)]. Here, island 2 has a thickness of four monolayers of silver while islands 1 and 3 are thicker islands on the surface. The islands 1 and 3 continue to grow while island 2 also starts to disintegrate [Fig. 4(c)]. Apparently, these metastable third and fourth layers are kinetically stabilized and become unstable (*partial dewetting* process) after reaching a certain critical coverage or, likewise, during a postanneal cycle when evaporation has already been stopped.

B. Lateral surface structure and film registry

The diffraction experiments using low-energy electrons were conducted after silver film preparation at growth temperatures between 500 and 850 K. The LEED images show the expected threefold symmetric diffraction pattern of the Ni(111) substrate with a weak moiré pattern, which is caused by the Ag(111) overlayer, essentially indicating the formation of a coincidence lattice comprised of individual sublattices of $(m \times m)$ and $(n \times n)$ translational periodicity, respectively. The determination of the in-plane scattering vectors $q_{\parallel}^{\mathrm{Ag,Ni}}$ of the integral order reflections for the Ni substrate and the Ag film from radial cuts through reciprocal space yields an in-plane lattice mismatch of $(15 \pm 2)\%$ between the silver film and the nickel substrate, in perfect accordance with the difference of 16% between the bulk lattice parameters of both materials. Hence, since silver essentially grows with its bulk lattice constant on the substrate, little lateral strain is imposed on the monolayer film.

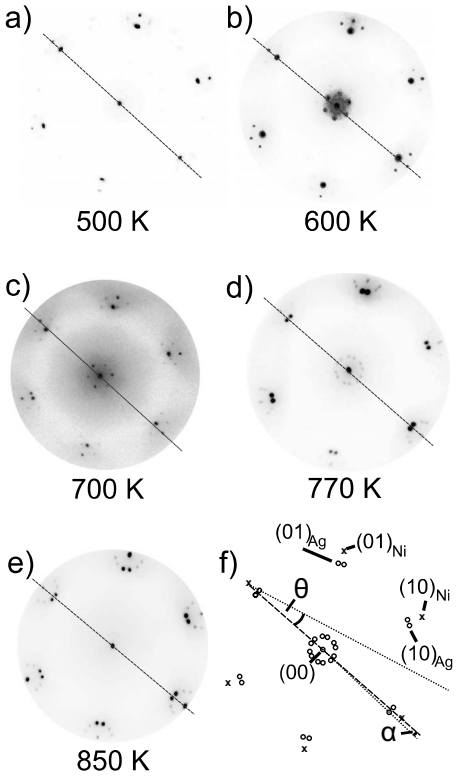

FIG. 5. The LEED images (a)–(e) were taken after preparation of silver films of about 2 ML thickness at different growth temperatures. The dashed lines connect the $(\bar{1}1)_{\mathrm{Ni}}$ and the $(1\bar{1})_{\mathrm{Ni}}$ reflexes. In (f) a schematic LEED image with the relevant reflections, the rotation angle α of the silver film relatively to the nickel substrate and the reconstruction angle θ according to the reconstruction nomenclature $(x \times y)R\theta$ is shown.

A closer look at the LEED patterns reveals a substantial qualitative difference with deposition temperature. At 500 and 600 K [cf. Figs. 5(a) and 5(b)], the moiré pattern is composed of two nonrotated sublattices of about $(6 \times 6)/(7 \times 7)$ periodicity, as predicted by Chambon *et al.*[36] based on quenched molecular-dynamics (QMD) simulations for this temperature range. However, elevated temperatures between 700 and 850 K induce an apparent splitting of the Ag integral order diffraction spots by about $\pm 2.2°$ from the main symmetry direction [Figs. 5(c)–5(e)], which is compatible with the existence of two rotational domains of $(\sqrt{52} \times \sqrt{52})R13.9°$ reconstructed areas [Fig. 5(f)]. Again, this experimental finding corroborates the QMD study by Chambon *et al.*, who attributed this structure to a coincidence lattice formed by the arrangement of 39 silver atoms and 52 nickel atoms within the surface unit mesh.

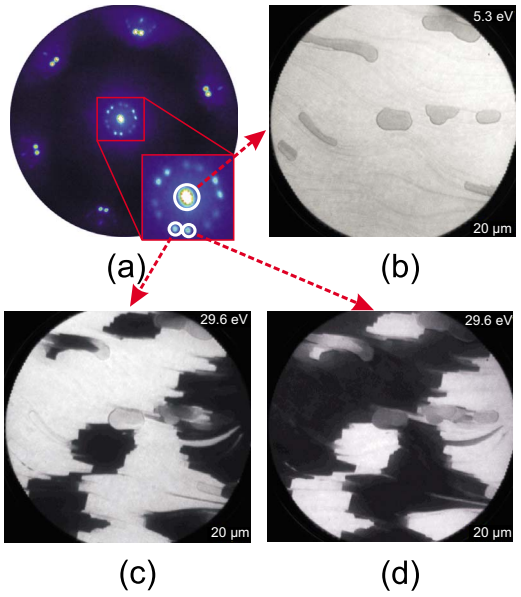

FIG. 6. (Color online) The LEED image taken at 47.8 eV electron energy in (a) shows the moiré pattern of the superlattice structure around the (00) spot. (b) Bright-field LEEM image employing the (00) diffraction peak for imaging. By tilting the incident electron beam, also distinct superlattice spots can be selected by the contrast aperture for imaging. The corresponding LEEM images are presented in (c) (dark field, first domain), and (d) (dark field, second domain). Sample prepared at about 800 K.

For other fcc-like bimetallic systems similar results are reported in the literature. On Cu(111),[9] silver forms both $(8\times8)/(9\times9)$ superstructures as well as rotated domains for deposition temperatures of about 370 K. A formation of twin domains has also been discovered for the systems Ag/Fe(110) (Ref. 12) and Ag/W(110).[13] Interestingly, despite the virtually identical lattice mismatch, a lateral compression of the Ag layer is not observed, which in the case of Au/Ni(111) induces the formation of an $(8\times8)/(9\times9)$ moiré pattern exhibiting an effective compressive strain of 2.8%. This important finding will be related to our results for the interface layer spacing between the Ag film and the Ni substrate (see Sec. IV C).

The concept of rotational domains for growth at higher temperatures such as 770 and 850 K can be proven in an elegant way by performing dark-field (DF) LEEM using the rotated superstructure spots for imaging [Fig. 6(a)] and comparing to the conventional bright-field image obtained by using the specular (00) reflection [Fig. 6(b)]. The bright-field LEEM image [Fig. 6(b)] shows the two monolayer thick silver wetting layer (bright) with some thicker silver islands (gray). As clearly observed from the dark-field LEEM images, which are presented in Figs. 6(c) and 6(d), the wetting layer is comprised of two distinct regions. By comparing both dark-field images it is evident that the images exhibit a complementary contrast apart from the thicker islands, which show up in both images. Furthermore, from the bright-field image it is evident that the wavy step edges essentially run from left to right. At first glance, the boundaries between the different rotational domains, which correspond to the two growth orientations of $\pm2.2°$ relative to the substrate lattice, seem to coincide with the step edges and step bunches of the substrate, but there are also short domain boundaries that extend in the direction (roughly up-down) normal to the steps. Since the sample was prepared at 800 K, the growth proceeds by step-edge decoration followed by subsequent island nucleation and growth. The large average size of the domains indicates that once an island nucleates with a certain registry to the substrate, it will spread over the available area until it hits another island of different rotational orientation, thereby creating the boundaries observed in DF-LEEM. The average shape of the domains reveals that the "native" domain boundaries coincide with step edges and should therefore be energetically favorable while the boundaries in the transverse direction tend to be shorter, suggesting thermodynamically less-favorable local atomic configurations. These explanations are in line with the growth behavior at high temperatures at which a flowlike decoration of step edges and terraces is witnessed. These points and its implications for the growth kinetics will be further discussed in Sec. IV D.

C. Vertical film and interface structure

A change in atomic structure—laterally and vertically—has a strong influence on the energy-dependent reflected intensity, the so-called $I(V)$ curve. Due to this fact, the incident layer structure can be determined by an optimization process of a model system in comparison to the experimental data as described in Sec. III.

In this work, we recorded profiles of the (00) beam reflection intensity vs electron voltage, i.e., the $I(V)$ spectra, of thin silver films at different Ag layer thicknesses and growth temperatures. For computational feasibility, the reference structure for the theoretical calculations was modeled by a laterally fully strained (1×1) reconstruction of the silver film adhering to the in-plane lattice constant of the Ni substrate. Although this assumption is not entirely realistic as discussed in Sec. IV B, very good agreement between experimental and theoretical $I(V)$ curves can already be achieved within this approximation in the very low-energy regime. Further justification for this structural model has been achieved by performing reference calculations for varied lateral lattice constants of the fully strained bimetallic system, ranging between the known Ag and Ni bulk lattice constants. In all cases, the vertical layer distances were found to be basically unaffected by the variation, rendering the determined values reliable to relatively high precision even within this approximation. We also note in passing that for $I(V)$ analyses in the limiting case of incommensurate overlayer structures the intensity of the specular beam is expected to be strongly sensitive to the interlayer spacing, but insensitive to the layer registry,[37] a fact that is already well established in the kinematic diffraction regime.

We introduce the theoretical model by first considering the clean Ni(111) substrate. The $I(V)$ curve of a certain region (marked by a black point) of the clean Ni(111) surface including the dynamical calculation is shown in Fig. 7. In the $I(V)$ calculation the tabulated bulk lattice constant of Ni(111) ($a=3.5232$ Å) (Ref. 38) was used, resulting in an excellent

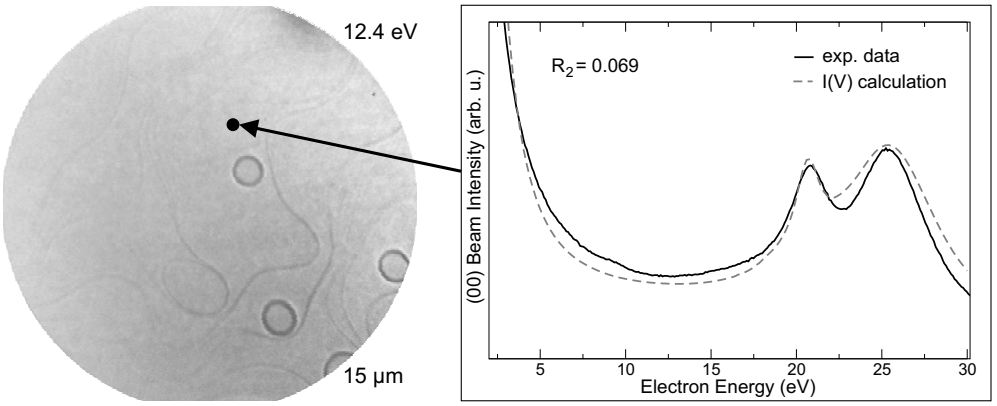

FIG. 7. LEEM image at 15 μm field of view and 12.4 eV electron energy with local $I(V)$ spectrum of the clean Ni(111) surface. The dark round objects in the LEEM image are insular elevations on the Ni crystal.

match to the experimental data, as documented by the low R_2 factor of 0.069. The intensity maximum at (25.4 ± 0.1) eV is identified with the Ni(111) Bragg peak while the peak at (20.6 ± 0.1) eV arises from in-plane multiple scattering involving local scattering events that are characterized by nonvanishing in-plane momentum transfer.

After silver deposition (and sometimes during deposition), $I(V)$ spectra were taken at points with different Ag layer thickness on the surface in an analogous fashion. The results including the corresponding dynamical calculations are shown in Fig. 8. For only one Ag layer on Ni(111) the $I(V)$ spectrum shows a broad intensity maximum between 13 and 20 eV that is attributed to the incoherent superposition of the emerging reflections of the monolayer silver film, which are significantly broadened due to the finite-size effect. Furthermore, the multiple-scattering peak of the Ni substrate and a distinct shoulder at (25.0 ± 0.5) eV, which marks the Ni(111) Bragg peak, are observed. For silver layer coverages $n \geq 2$ the intensities of the silver peaks become stronger, which is accompanied by a decreasing width. Moreover, the oscillations due to the QSE (Ref. 27) are most pronounced in the energy range between 2 and 13 eV. The in-plane multiple-scattering reflection of the Ag layers is located at (13.5 ± 0.5) eV, followed by the Bragg peak of the silver film at (17.5 ± 0.5) eV. Obviously, all these features bear information on the atomic structure of the Ag film and the interface. However, since only the (00) reflected beam is analyzed, the model is mostly sensitive to the vertical alignment of the atomic layers while information on lateral structure only enters by higher-order terms in multiple scattering.

By modeling the $I(V)$ spectra obtained for ultrathin Ag films the interface distance, which is the distance between the undermost silver layer and the Ni substrate, is determined to (2.8 ± 0.1) Å. This stands in very good agreement with the results of Trontl *et al.*[20] and, very recently, of Aït-Mansour and Gröning,[18] who for a monolayer of silver on Ni(111) reported step heights of (2.87 ± 0.05) Å and 2.74 Å by scanning tunneling microscopy, respectively. Interestingly, we do not observe a dependence of the interface layer spacing on the silver film thickness as found for the system Ag/W(110) by $I(V)$-LEED.[39] We also note that we do not find any evidence for stacking-fault formation as in the related case of Au/Ni(111).[16] Together with the LEED observations, which demonstrate the absence of a significant amount of in-plane strain in the overlayer, our $I(V)$-LEED results indicate an almost perfect decoupling of the Ag film from the underlying Ni crystal.

The seemingly large error of ± 0.1 Å reflects the small number of intensity features in the spectra of the one and two monolayer silver films used in our calculation. In case of $n > 2$ Ag layers the vertical distance between the silver layers amounts to (2.35 ± 0.03) Å, in perfect agreement with the lattice constant of bulk Ag(111). For the distance of the Ag top layer to the second silver layer we find a systematic contraction of about 0.1 Å with respect to the bulk lattice constant, indicating a surface relaxation of $(4.4 \pm 1.0)\%$ in the ultrathin film (cf. Table I). This general phenomenon is very well known for surfaces of metal crystals and has been determined for a variety of different metallic surfaces.[40–42] The calculation of the real reconstruction as identified by

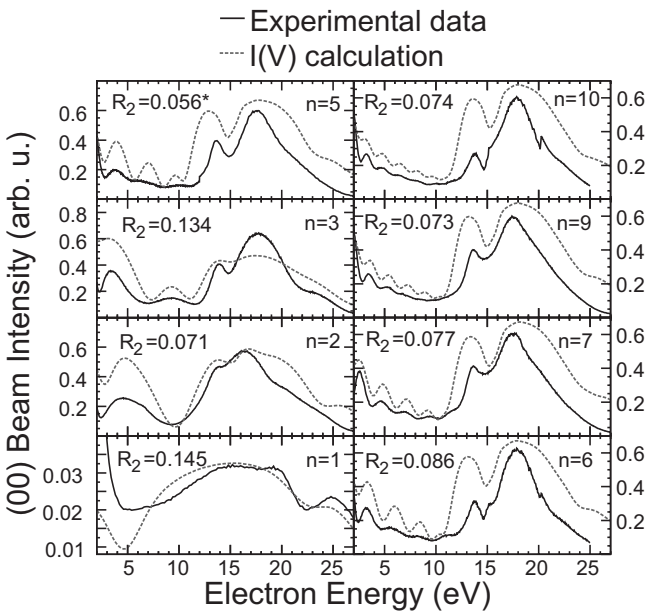

FIG. 8. Experimental $I(V)$ characteristics and theoretical calculations of thin silver films of $n=1$ to $n=10$ Ag layer thickness. The R_2 factors are calculated over the whole region shown here. For $n=5$ (*) the R_2 factor has been determined for the range from 2 to 15 eV due to discontinuities in the experimental data set.

TABLE I. Model parameter for the $I(V)$ calculations. The interlayer distance in [111] direction between the uppermost and the subjacent silver layer is labeled by d_{12}, the distance between the last silver monolayer and the Ni substrate by d_{int}.

Number of Ag monolayers	d_{12} (Å)	d_{int} (Å)
Pure Ni(111)	2.03 ± 0.03	
1	2.80 ± 0.10	
2	2.33 ± 0.03	2.80 ± 0.10
3	2.28 ± 0.03	2.80 ± 0.10
5	2.25 ± 0.03	2.87 ± 0.10
6	2.23 ± 0.03	2.80 ± 0.10
7	2.24 ± 0.03	2.87 ± 0.10
9	2.25 ± 0.03	2.87 ± 0.10
10	2.25 ± 0.03	2.87 ± 0.10
12	2.25 ± 0.03	2.87 ± 0.10

LEED (Sec. IV B) would mainly affect the energetic position of the in-plane multiple-scattering peak of the Ag film while the remaining reflections would not significantly be affected.

Lastly, our $I(V)$ analysis allows us to investigate potential alloying of the silver adsorbate with the nickel substrate. For this purpose, we considered different mixing ratios (between 10% and 90% of Ag) of Ag and Ni in the top layers. However, based on the results of these calculations and subsequent comparison to the experimental $I(V)$ data (not shown) alloy formation can completely be ruled out. Nor is surface alloy formation evident in the *in situ* LEEM experiments in which the effect of high-temperature annealing close to the desorption temperature was studied.

D. Interplay of strain and growth kinetics

In this section, we provide details on the growth mode that are only accessible with *in situ* methods. We start by analyzing the formation of the first and second Ag adlayer depending on substrate temperature and deposition time. In Fig. 9 the coherent Ag coverage as determined by LEEM, i.e., the fraction of available surface area covered by nucleated Ag islands of monolayer height, is plotted as a function of deposition time for two growth temperatures (600 K and 750 K) and two apparently different evaporator fluxes (0.30 ± 0.03 and 0.64 ± 0.06 ML/min), which have been determined by extrapolation of the growth rate at low coverages. In the submonolayer regime, a negative curvature is visible for all data sets. After nucleation and island formation starting at the step edges (cf. Sec. IV A), the terraces are gradually filled with Ag islands. However, with decreasing available surface area for Ag island formation the apparent growth rate seems to slow down. Since the deposition rate was kept fixed during the experiment, the amount of Ag on the surface must nevertheless be higher than the fraction of surface area covered by the islands. Hence, the remaining Ag atoms that are not incorporated into the islands should be randomly distributed on the Ni terraces or on top of the Ag monolayer, undergoing thermally activated processes such as surface diffusion as well as metastable island attachment and

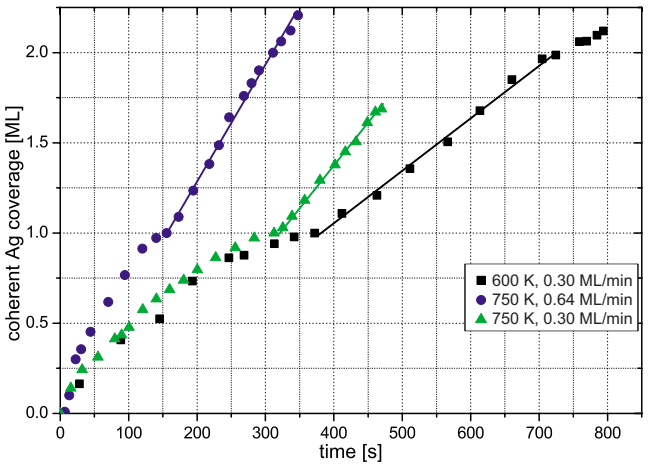

FIG. 9. (Color online) The coherent Ag coverage over time has been extracted from the LEEM growth movies at constant electron energy and image focus. While the first monolayer grows, the apparent deposition rate decreases with increasing silver coverage due to strain effects.

detachment until finally getting permanently bonded to existing islands. Again, this scenario agrees with the identification of strain release as the underlying reason for the dendritic island shape (see Sec. IV A) since the rates for adatom capture and detachment should be fairly comparable according to the large fraction of Ag atoms in the lattice-gas phase.

To prove the idea of the existence of a transient phase,[43] also termed "lattice gas" in the literature, we tried to freeze the surface in this state of submonolayer coverage and analyzed the local Ag coverage by performing microspectroscopy in PEEM mode in the near-valence-band regime. Typical local valence-band spectroscopy data for supposedly uncovered and Ag-covered regions are displayed in Fig. 10. As can be rationalized by comparing the peak intensities of the Ag $4d$ band, even the nominally silver-free regions exhibit a substantial Ag concentration in the order of about 20% of a monolayer.

The amount of Ag forming the lattice gas may also be estimated from the area enclosed between the coverage curves and the linear relation that would symbolize a growth rate reflecting the true deposit per time. Indeed, such a numerical evaluation yields Ag fractions ranging from about 18–22 %, in perfect agreement with the previous determination from valence PEEM.

In the absence of obvious kinetic effects due to the comparable Ag fluxes employed, a possible reason for the

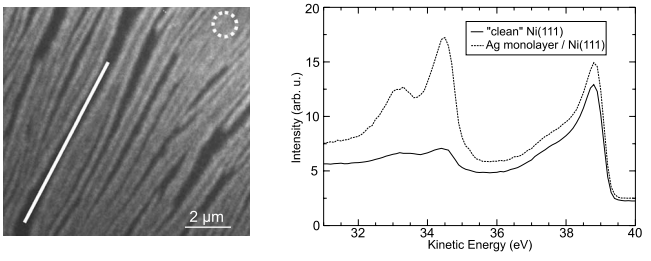

FIG. 10. Left: valence-band PEEM image ($E=13.5$ eV) taken after Ag growth at 850 K. Right: local valence-band spectra at regions indicated in PEEM image.

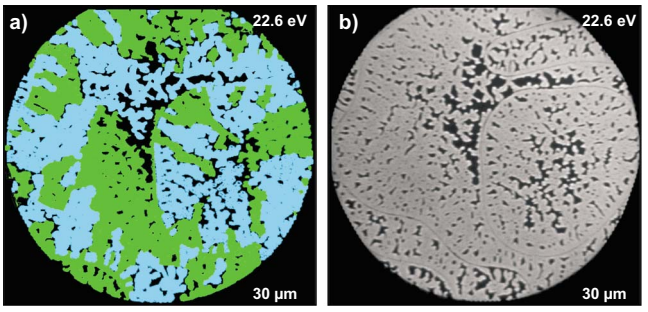

FIG. 11. (Color online) (a) Composite LEEM image (E =22.6 eV) consisting of two dark-field LEEM images (blue and green) using superstructure spots as in Fig. 6 revealing the lateral distribution of rotational domains after Ag submonolayer growth at 750 K. (b) Bright-field LEEM image (E=22.6 eV) of the same area.

temperature-dependent growth behavior should be related to thermodynamical arguments. Among these, surface strain seems to be most likely in light of the fact that two different reconstructions are observed for the respective temperature regimes as evidenced by LEED (Sec. IV B). The $(6\times6)/(7\times7)$ structure, which prevails for lower temperatures, can be expected to exhibit higher amounts of strain than the rotated $(\sqrt{52}\times\sqrt{52})R13.9°$ reconstruction. Since the release of strain should be easier for smaller coherently covered areas, island growth is impeded especially for lower temperatures.

The strain fields surrounding the islands mediate the interaction between neighboring two-dimensional Ag islands, leading to remarkable effects at silver coverages close to a full monolayer. In Fig. 11, a dark-field analysis of the lateral distribution of the rotational domains is shown for the sample prepared at 750 K whose growth sequence is displayed in Fig. 2, albeit here at a later stage when the silver film is almost closed. It is evident that the largest areas not covered by silver islands are found not only between crystallographically inequivalent rotational domains but also between rotational domains exhibiting the same angle with respect to the main symmetry directions of the substrate. These findings yet again illustrate that the dendritic island shape should indeed be responsible for interfacial strain release and that orientational misalignment between the individual domains, which could, in principal, result in a higher degree of disorder and thus higher energy costs at their mutual boundaries, only plays a minor role. Together with the previous observations regarding the lattice gas, we find overwhelming evidence for surface strain being the fundamental driving force governing both nucleation and growth phenomena for Ag/Ni(111).

V. CONCLUSION

We have presented a comprehensive low-energy electron microscopy study of the growth mode, the morphology and the atomic structure of ultrathin silver films on Ni(111) depending on substrate temperature. After the initial growth phase, consisting of either nucleation at terraces ($T<500$ K) or step-edge decoration followed by island growth onto terraces ($T>500$ K), the silver grows in the Stranski-Krastanov growth mode with a wetting layer of two monolayer thickness. Throughout the whole temperature range up to 800 K the silver islands exhibit a dendritic growth morphology. Temperatures of 500 K lead to a nucleation on the Ni(111) terraces and after longer evaporation to a multitude of different silver layer thicknesses on the wetting layer. Higher temperatures of more than 700 K lead to a lamellar growth of silver along the step edges and after a longer time of evaporation to very thick Ag islands.

The theoretical analysis using multiple-scattering theory of the intensity-voltage spectra obtained in LEEM mode shows that the distance between the nickel substrate and the silver film amounts to (2.8 ± 0.1) Å for all film thicknesses (number of layers $1\leq n\leq12$) investigated. Furthermore, the individual silver layers grow with the bulk lattice constant of Ag(111), pointing toward effective strain relaxation because of the high silver-nickel distance at the interface. Only the uppermost Ag layer of Ag films of $n>2$ layers exhibits a vertical distance that is $(4.4\pm1.0)\%$ shorter as compared to the bulk value.

However, residual strain still plays a major role for the growth and nucleation phenomena at lower temperatures, especially between 500 and 700 K. In this regime, the silver film grows in a $p(7\times7)$ structure as verified from the moiré pattern observed in diffraction mode. This reconstruction is not found for higher deposition temperatures, for which a $(\sqrt{52}\times\sqrt{52})R13.9°$ with two crystallographically inequivalent rotational domains is formed in the whole temperature range up to 850 K. These findings indicate that the $p(7\times7)$ reconstruction features a higher level of strain, which using LEEM and PEEM has been shown to result in substantially enhanced adatom gas formation for few-layer deposits as compared to the high-temperature regime, in which the $(\sqrt{52}\times\sqrt{52})R13.9°$ reconstruction prevails.

ACKNOWLEDGMENTS

The authors would like to thank Jurek Sadowski, Percy Zahl, Peter Sutter (Center for Functional Nanomaterials, BNL), and Gary Nintzel (NSLS, BNL) for technical support. Research was carried out in part at the Center for Functional Nanomaterials, Brookhaven National Laboratory, which is supported by the U. S. Department of Energy, Office of Basic Energy Sciences, under Contract No. DE-AC02-98CH10886.

*flege@ifp.uni-bremen.de

[1] J. G. Chen, C. A. Menning, and M. B. Zellner, Surf. Sci. Rep. **63**, 201 (2008).

[2] X. J. Liu, F. Gao, C. P. Wang, and K. Ishida, J. Electron. Mater. **37**, 210 (2008), and references therein.

[3] A. Varykhalov, A. M. Shikin, W. Gudat, P. Moras, C. Grazioli, C. Carbone, and O. Rader, Phys. Rev. Lett. **95**, 247601 (2005).

[4] P. A. Montano, P. P. Vaishnava, and E. Boling, Surf. Sci. **130**, 191 (1983).

[5] A. Nilsson, M. A. Morris, and D. Chadwick, Surf. Sci. **152-153**, 247 (1985).

[6] D. O. Boerma, G. Dorenbos, G. H. Wheatley, and T. M. Buck, Surf. Sci. **307-309**, 674 (1994).

[7] L. Pleth Nielsen, F. Besenbacher, I. Stensgaard, E. Lægsgaard, C. Engdahl, P. Stoltze, K. W. Jacobsen, and J. K. Nørskov, Phys. Rev. Lett. **71**, 754 (1993).

[8] J. Jacobsen, L. Pleth Nielsen, F. Besenbacher, I. Stensgaard, E. Lægsgaard, T. Rasmussen, K. W. Jacobsen, and J. K. Nørskov, Phys. Rev. Lett. **75**, 489 (1995).

[9] W. E. McMahon, E. S. Hirschorn, and T.-C. Chiang, Surf. Sci. **279**, L231 (1992).

[10] M. Wessendorf, C. Wiemann, M. Bauer, M. Aeschlimann, M. A. Schneider, H. Brune, and K. Kern, Appl. Phys. A: Mater. Sci. Process. **78**, 183 (2004).

[11] W. L. Ling, J. de la Figuera, N. C. Bartelt, R. Q. Hwang, A. K. Schmid, G. E. Thayer, and J. C. Hamilton, Phys. Rev. Lett. **92**, 116102 (2004).

[12] H. Noro, R. Persaud, and J. A. Venables, Vacuum **46**, 1173 (1995).

[13] J. A. Venables, D. R. Batchelor, M. Hanbucken, C. J. Harland, and G. W. Jones, Philos. Trans. R. Soc. London, Ser. A **318**, 243 (1986).

[14] L. Pleth Nielsen, F. Besenbacher, I. Stensgaard, E. Lægsgaard, C. Engdahl, P. Stoltze, and J. K. Nørskov, Phys. Rev. Lett. **74**, 1159 (1995).

[15] J. J. Paggel, T. Miller, and T.-C. Chiang, Science **283**, 1709 (1999).

[16] K. Umezawa, S. Nakanishi, and W. M. Gibson, Phys. Rev. B **57**, 8842 (1998).

[17] C. Chambon, A. Coati, and Y. Garreau, Surf. Sci. **602**, 2363 (2008).

[18] K. Aït-Mansour and O. Gröning, Surf. Sci. **604**, 872 (2010).

[19] C. Chambon, A. Coati, and Y. Garreau, Surf. Sci. **604**, 875 (2010).

[20] V. M. Trontl, P. Pervan, and M. Milun, Surf. Sci. **603**, 125 (2009).

[21] S. Nakanishi, K. Umezawa, M. Yoshimura, and K. Ueda, Phys. Rev. B **62**, 13136 (2000).

[22] K. Meinel, O. Lichtenberger, and M. Klaua, Phys. Status Solidi A **116**, 47 (1989).

[23] S. Mróz and Z. Jankowski, Surf. Sci. **322**, 133 (1995).

[24] J. I. Flege, E. Vescovo, G. Nintzel, L. H. Lewis, S. Hulbert, and P. Sutter, Nucl. Instrum. Methods Phys. Res. B **261**, 855 (2007).

[25] V. Blum and K. Heinz, Comput. Phys. Commun. **134**, 392 (2001).

[26] J. Sun, J. B. Hannon, G. L. Kellogg, and K. Pohl, Phys. Rev. B **76**, 205414 (2007).

[27] M. S. Altman, W. F. Chung, and C. H. Liu, Surf. Rev. Lett. **5**, 1129 (1998).

[28] T. A. Witten, Jr. and L. M. Sander, Phys. Rev. Lett. **47**, 1400 (1981).

[29] T. A. Witten and L. M. Sander, Phys. Rev. B **27**, 5686 (1983).

[30] R. Q. Hwang, J. Schröder, C. Günther, and R. J. Behm, Phys. Rev. Lett. **67**, 3279 (1991).

[31] T. Michely, M. Hohage, M. Bott, and G. Comsa, Phys. Rev. Lett. **70**, 3943 (1993).

[32] H. Brune, C. Romainczyk, H. Röder, and K. Kern, Nature (London) **369**, 469 (1994).

[33] Z. Zhang, X. Chen, and M. G. Lagally, Phys. Rev. Lett. **73**, 1829 (1994).

[34] M. Hohage, M. Bott, M. Morgenstern, Z. Zhang, T. Michely, and G. Comsa, Phys. Rev. Lett. **76**, 2366 (1996).

[35] W. Wulfhekel, F. Zavaliche, R. Hertel, S. Bodea, G. Steierl, G. Liu, J. Kirschner, and H. P. Oepen, Phys. Rev. B **68**, 144416 (2003).

[36] C. Chambon, J. Creuze, A. Coati, M. Sauvage-Simkin, and Y. Garreau, Phys. Rev. B **79**, 125412 (2009).

[37] H. Zi-Pu, D. F. Ogletree, M. A. V. Hove, and G. A. Somorjai, Surf. Sci. **180**, 433 (1987).

[38] P. Villars and L. D. Calvert, *Pearson's Handbook of Crystallographic Data for Intermetallic Phases* (ASM International, Metal Parks, Ohio, 1985), Vol. 3.

[39] H. C. Poon, S. Y. Tong, W. F. Chung, and M. S. Altman, Surf. Rev. Lett. **5**, 1143 (1998).

[40] M. L. Xu and S. Y. Tong, Phys. Rev. B **31**, 6332 (1985).

[41] J. de la Figuera, J. M. Puerta, J. I. Cerda, F. E. Gabaly, and K. F. McCarty, Surf. Sci. **600**, L105 (2006).

[42] J. Wan, Y. L. Fan, D. W. Gong, S. G. Shen, and X. Q. Fan, Modell. Simul. Mater. Sci. Eng. **7**, 189 (1999).

[43] J. A. Venables, G. D. T. Spiller, and M. Hanbücken, Rep. Prog. Phys. **47**, 399 (1984).